Electrocatalysis in confinement: metal-organic frameworks for oxygen reduction

Hoefnagel, M.E.

Chapter 2

Directing the Selectivity of Oxygen Reduction to Water by Confining a Cu Catalyst in a Metal-Organic Framework

Electrocatalysis is to play a key role in the transition towards a sustainable chemical and energy industry and active, stable and selective redox catalysts are much needed. Porous structures such as metal-organic frameworks (MOFs) are interesting materials as these may influence selectivity of chemical reactions through confinement effects. In this work, we incorporate the oxygen reduction catalyst Cu-tmpa into the NU1000 MOF. Confinement of the catalyst within NU1000 steers the selectivity of the oxygen reduction reaction (ORR) towards water rather than peroxide. This is attributed to retention of the obligatory H_2O_2 intermediate in close proximity to the catalytic center. Moreover, the resulting NU1000|Cu-tmpa MOF shows excellent activity and stability in prolonged electrochemical studies, illustrating the potential of this approach.

This chapter was published as an article: M. E. Hoefnagel, D. Rademaker, D. G. H. Hetterscheid, *ChemSusChem* **2023**, *16*, e202300392.

2.1 Introduction

Catalysis will contribute largely to modernization of the chemical industry as it facilitates making carbon-neutral fuels and making industrial chemical processes more sustainable. Electrocatalysis in specific is expected to play a key role in the replacement of fossil fuels and polluting chemistry by sustainable alternatives.[1–3] Key characteristics that make a good catalyst are activity, stability and selectivity. Porous materials, such as zeolites, porous carbon materials, covalent organic frameworks (COFs) and metal organic frameworks (MOFs) have shown to affect the selectivity by so-called confinement effects.[4–8] These confinement effects include the diffusion of substrate and arrangement of substrate relative to the catalytic center, as well as spatial arrangement of catalytic centers relative to each other.[9] Geometrical constraints caused by pore size have shown to enable enantiomeric and chiral selectivity.[10,11] Moreover, the influence of neighboring groups to the catalytic center and hydrophilicity effects can alter affinity for substrates.[12–14] MOFs in particular offer a well-defined environment that allows for a high degree of tunability.

A catalytic reaction for which directing selectivity is of great importance is the oxygen reduction reaction (ORR), which is currently limiting the efficiency of fuel cells. The most commonly used catalyst for ORR in fuel cells is platinum. Due to Pt scarcity, ORR catalysts based on abundant first-row transition metals are a focus of investigation. The ORR can either proceed via the 4-electron reduction to water (Equation 1) or via a 2-electron reduction to hydrogen peroxide (Equation 2), which then can be further reduced to water (Equation 3). Hydrogen peroxide formed during the ORR can cause significant degradation of fuel cell membranes, and its formation should be avoided.[15]

$$O_2 + 4e^- + 4H^+ \longrightarrow 2H_2O \quad (1)$$

$$O_2 + 2e^- + 2H^+ \longrightarrow H_2O_2 \quad (2)$$

$$H_2O_2 + 2e^- + 2H^+ \longrightarrow 2H_2O \quad (3)$$

Many molecular oxygen reduction catalysts have been studied in the past three decades, which are largely based on complexes of porphyrins and phtalocyanines, as well as pyridine-based ligands of the first row transition metals cobalt, iron, manganese and copper.[16–22] Amongst homogeneous oxygen reduction catalysts, one of the fastest electrocatalysts reported thus far is copper(II) tris(2-pyridylmethyl)amine (Cu-tmpa), with a TOF_{max} of 1.8×10^6 s^{-1}.[23–28] Oxygen reduction by Cu-tmpa is initiated by reduction of Cu^{II} to Cu^{I}, followed

by binding of dioxygen to the Cu^{I} species in the rate determining step. Subsequently, a proton-coupled electron transfer is followed by a proton transfer that releases hydrogen peroxide as an isolable intermediate (eq. 2). Hydrogen peroxide is reduced by Cu-tmpa in a slower process (2.1×10^5 s^{-1}) that presumably occurs via a homolytic scission of the O-O bond at a reduced Cu^{I} site,[28] and formation of a hydroxyl radical. Further reduction leads to the formation of water as the product.

Several methods have been reported for the immobilization of molecular catalysts in MOFs.[29] The catalyst can for example be trapped in a MOF pore that acts as a cage (the 'ship-in-a-bottle' method),[30,31] a MOF linker can act as an anchor for the catalyst, as applied in the UiO MOF series,[32,33] or the catalyst itself is the linker within the MOF, as seen in the widely applied PCN series with porphyrinic units.[34–37] Additionally, a molecular catalyst can be incorporated into a MOF upon coupling a functional group in the periphery of the catalyst with terminal hydroxyl ligands present on the nodes by solvent-assisted ligand incorporation (SALI).[38–40] The stable NU1000 MOF contains hydroxyl ligands on its Zr-nodes, making it suitable for such a SALI approach. Incorporating a catalyst by SALI allows it to retain its structure and its dynamics, while dimerization reactions and detachment from the electrode are prevented.[41–45] Given that the catalyst flexibility is of great importance for rapid ORR catalysis at single-site copper species,[46,47] the SALI method is deemed as the most optimal. So far, catalysts that have been incorporated into MOFs by SALI include a nickel catalyst for ethylene dimerization,[48] an iridium catalyst for ethylene hydrogenation,[49] an iron porphyrin catalyst for photochemical CO_2 reduction,[50] and molybdenum sulfide for electrocatalytic hydrogen evolution.[51] A handful of MOFs, mainly with redox active linkers, for ORR have been studied and were found to favor hydrogen peroxide as the main product.[34,37,52–54] In general the long term performance of these MOFs is mediocre; current losses of 10-50% were observed in periods over three to six hours of electrolysis, or no stability data was provided whatsoever. In this work we have incorporated a carboxylic acid modified variation of the fast oxygen reduction catalyst Cu-tmpa into the NU1000 MOF by SALI and have studied its electrocatalytic ORR activity. We show that the NU1000|Cu-tmpaCOOH MOF retains its catalytic performance during 6 hour electrolysis experiments and recycling experiments (5×6 hours). Moreover, it selectively forms H_2O as the ORR product, showing that the confinement of the catalyst within this MOF fully directs its selectivity towards water.

2.2 Results

2.2.1 Synthesis

Synthesis of NU1000|Cu-tmpaCOOH

In order to incorporate the catalyst in the MOF pores, a tris(2-pyridylmethyl)amine (tmpa) ligand was functionalized with a carboxylic acid group by a three-step synthesis (See chapter 2.5 for experimental details). In the first step, the primary alcohol of methyl 6-hydroxymethylnicotinate was oxidized to an aldehyde by Dess-Martin oxidation. In the second step, the aldehyde was attached to bis(pyridin-2-ylmethyl)amine in a reductive amination to form the carboxylate-substituted tripodal tmpa ligand. In the last step, the methyl ester was hydrolyzed to a carboxylic acid using LiOH in a THF/H_2O mixture. The tmpaCOOH ligand was coordinated to $Cu(OTf)_2$ to obtain [Cu-tmpaCOOH(OTf)](OTf), as confirmed by elemental analysis, HRMS (section 2.5) and EPR (section 2.2.2). Moreover, Evans NMR showed an effective magnetic moment μ_{eff} = 1.95, corresponding to one unpaired electron as expected for Cu^{II}. The linker 4,4',4'',4'''-(pyrene-1,3,6,8-tetrayl)tetrabenzoic acid (TBAPy) was synthesized by a Suzuki coupling and the NU1000 MOF by solvothermal synthesis, both described in literature.[55] The successful formation of NU1000 was confirmed by PXRD, N_2-adsorption isotherm and SEM measurements (Section 2.2.2). The catalyst was loaded into NU1000 pores by SALI; the MOF was soaked in a 0.1 M solution of Cu-tmpaCOOH in DMF at 60 °C for 30 days.[39] Incorporation of the catalyst was confirmed by N_2-absorption isotherm, FT-IR, ICPMS and EPR (Section 2.2.2).

Synthesis of NU1000|Cu(OTf)$_2$

It has previously been reported that incorporation of Cu complexes into NU1000 may generate Cu-nanoparticles, which have been shown to be active in the CO_2 reduction reaction.[56] In order to verify whether any catalysis initiated by NU1000|Cu-tmpaCOOH MOF should be attributed to Cu-nanoparticles, Cu was incorporated into NU1000 by soaking NU1000 in a 0.1 M solution of $Cu(OTf)_2$ in DMF for 10 days. The Cu loading for this NU1000|$Cu(OTf)_2$ sample was determined with ICPMS (Section 2.2.2).

2.2.2 Characterization

The synthesized MOF and the Cu-tmpaCOOH-treated MOF were characterized by powder X-ray diffraction (XRD), N_2-adsorption isotherm, scanning electron microscopy (SEM),

Fourier-transform infrared spectroscopy (FT-IR), electron paramagnetic spectroscopy (EPR) and inductively coupled plasma mass spectrometry (ICPMS).

Powder X-Ray Diffraction

XRD was measured to characterize MOF structure before and after incorporation of the catalyst (**Figure *2.1***). Spectra are in good agreement with a simulated spectrum for NU1000 and spectra reported in literature.[38,57]

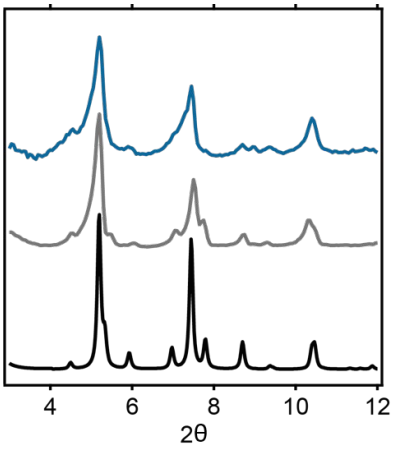

Figure 2.1 PXRD patterns of NU1000 (grey) and NU1000|Cu-tmpaCOOH (blue) and simulated XRD pattern[38] of NU1000 (black).

N_2 adsorption isotherm

N_2 adsorption and desorption were measured to characterize the MOF porosity and the resulting data were treated with BELMaster software to obtain pore size distributions for micropores and macropores (Figure 2.2). The typical NU1000 values for small pores of 10 Å and larger pores of 22.6 Å were found. For the macropores of NU1000, a pore width of 31 Å is generally reported, but when moieties are incorporated into the pores by SALI, pore size decreases.[38,39] The large NU1000 pores were reported to decrease to 27.5 Å upon incorporation of alkanes and to 28 Å and 26 Å for incorporation of isonicotinic acid and iodobenzoic acid, respectively. Therefore, we attribute the peak of 22.6 Å to the large NU1000 pore with Cu-tmpaCOOH incorporated. The peak has an inhomogeneous character as, at a loading of 1.4 Cu per node, some pores contain one catalyst while others contain two.

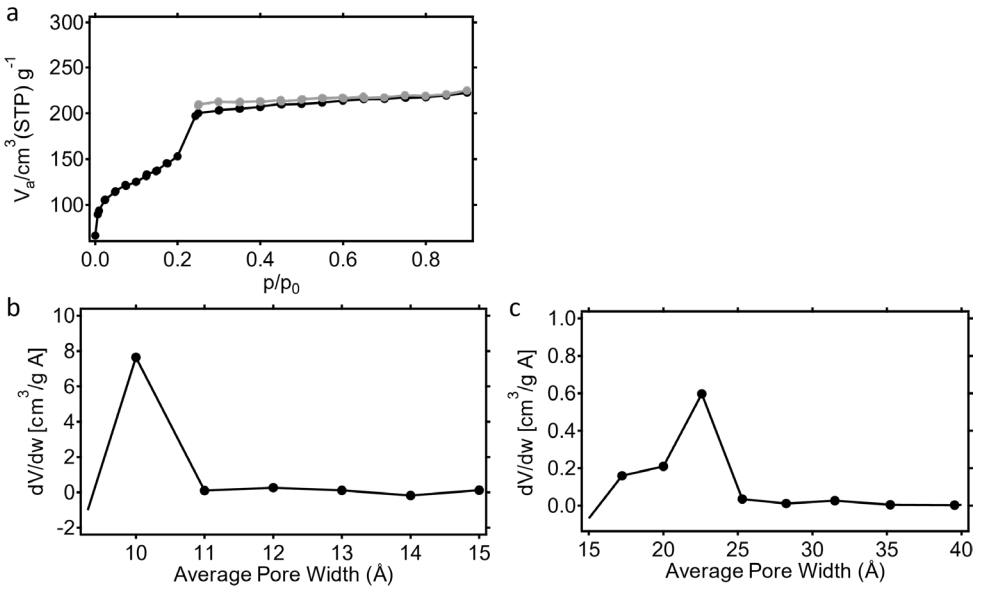

Figure 2.2 N_2 adsorption (a, black line) and desorption (a, grey line) and calculated MP micro pore size (b) and BJH macro pore size (c) of NU1000|Cu-tmpaCOOH.

Scanning Electron Microscopy

MOF morphology was characterized by scanning electron microscopy (SEM) at a working distance of 8 mm and a zoom of 2500 to 5000 times. SEM was measured for NU1000 (Figure 2.3a) NU1000|Cu-tmpaCOOH (Figure 2.3b) NU1000|Cu-tmpaCOOH drop casted with carbon black (Figure 2.3c) and NU1000|Cu-tmpaCOOH drop casted with carbon black after catalytic experiments (Figure 2.3d). SEM images show the MOF having typical NU1000 hexagonal rods, and it was found that the morphology does not change during catalysis.[40,57]

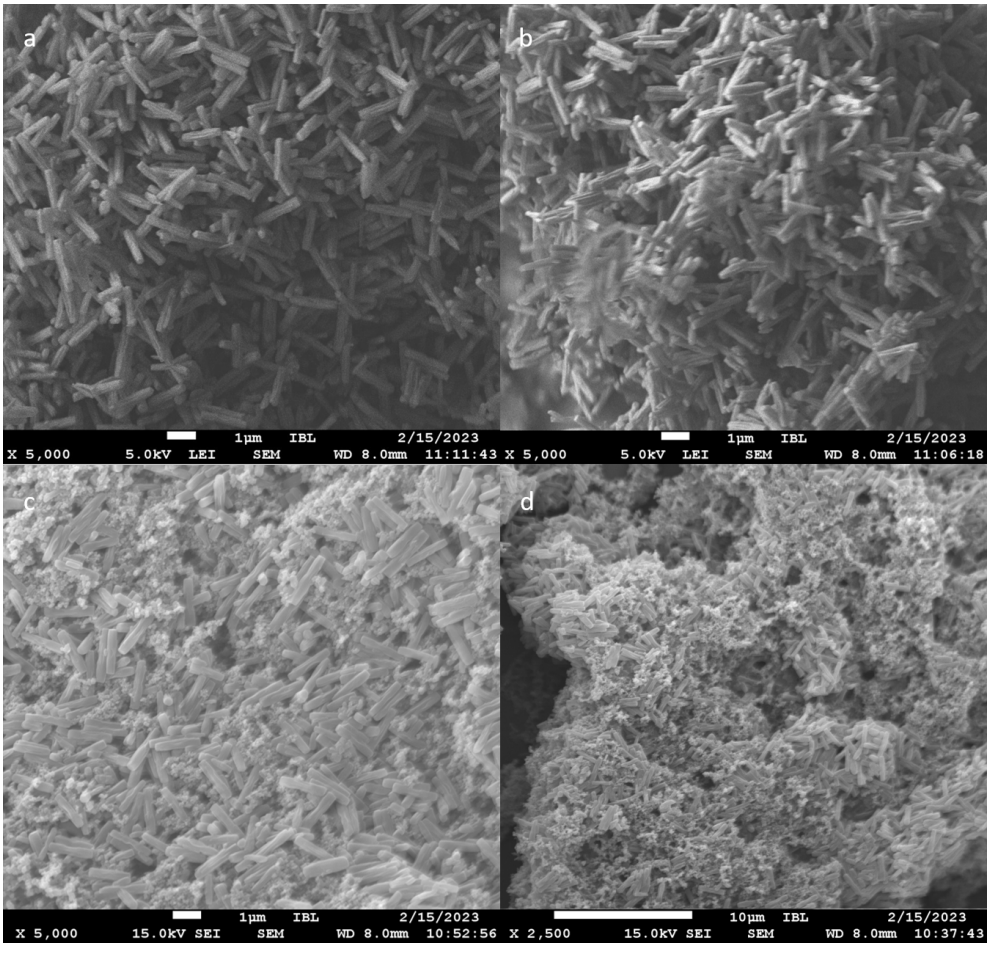

Figure 2.3 SEM images of (a) NU1000, zoom 5000x, (b) NU1000|Cu-tmpaCOOH, zoom 5000x, (c) NU1000|Cu-tmpaCOOH drop casted with carbon black and Nafion® before CA, zoom 5000x, (d) NU1000|Cu-tmpaCOOH drop casted with carbon black and nafion after 6h CA, zoom 2500x.

Fourier-transform Infrared Spectroscopy

FT-IR was measured of NU1000 before (Figure 2.4, black line) and after SALI (Figure 2.4, blue line). The FT-IR spectrum of NU1000 after SALI shows a C=O stretch peak (±1656 cm^{-1}) that is assigned to the carbonyl of the bond formed between the catalyst and the MOF node.

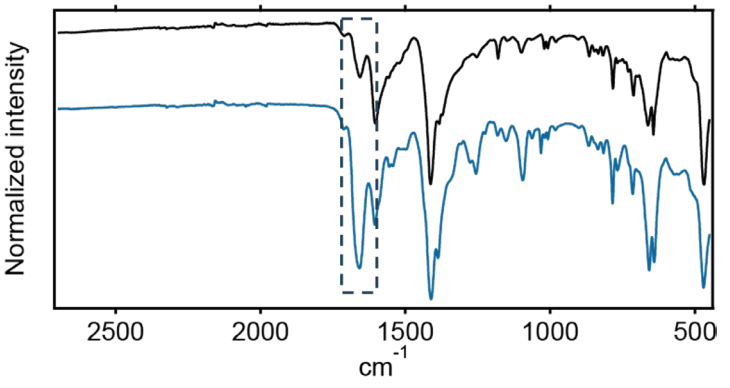

Figure 2.4 FTIR spectra of NU1000 powder (black) and NU1000|CutmpaCOOH powder (blue). The spectrum for NU1000|Cu-tmpaCOOH has a peak at 1656 cm^{-1}, which is assigned to the carbonyl in the bond between the catalyst and node.

Electron Paramagnetic Resonance

EPR spectra of Cu-tmpa, Cu-tmpaCOOH and NU1000|Cu-tmpaCOOH were recorded at 130 K under continues N_2 flow in quartz glass EPR tubes. The EPR spectrum of Cu-tmpa matches very well with the spectrum previously reported (Figure 2.5).[58] The EPR spectrum of Cu-tmpaCOOH does not show a hyperfine coupling in contrast to the spectrum of Cu-tmpa and appears to be isotropic. This may be due to intermolecular interactions between the Cu-site and the carboxylic acid moiety. The EPR spectrum of NU1000|Cu-tmpaCOOH matches well with that of Cu-tmpa apart of some broadening and illustrates that a single site Cu-tmpa unit has been successfully incorporated within the MOF.

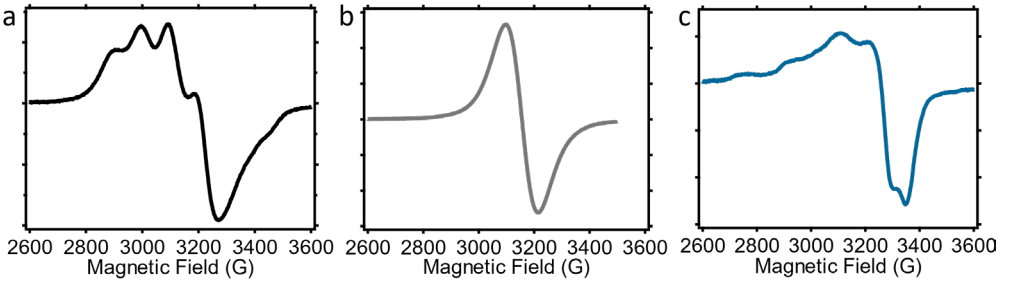

Figure 2.5 EPR spectra of Cu-tmpa (a), Cu-tmpaCOOH (b) and NU1000|Cu-tmpaCOOH (c).

Inductively Coupled Plasma Mass Spectrometry

ICPMS samples were prepared by digesting MOF in nitric acid at elevated temperature and subsequent dilution with MilliQ water. The concentrations of Zr and Cu ions (in parts per

billion) were determined in triplicate and the results shown in Table A1. From these values, the ratio of Zr : Cu can be calculated. As one NU1000 node contains six Zr ions, we can use the Zr : Cu ratio to calculate the number of Cu-centers per node (Table 2.1). Carbon black, which was used as an additive for electrochemical experiments on the MOF, was analyzed by ICPMS to exclude metal impurities and the results are shown in Table A2. ICPMS showed loadings that varied between 0.8 to 1.4 Cu-tmpaCOOH units per node. The MOF with a loading of 1.4 was used for electrochemical experiments, unless noted otherwise.

Table 2.1 Average Zr and Cu contents (ppb) of NU1000|Cu-tmpaCOOH and NU1000|$Cu(OTf)_2$ as determined by ICPMS measurements.

Sample ID	Zr : Cu	Catalysts per node [a]
NU1000|Cu-tmpaCOOH batch 1	4 : 1	1.4 (±0.1)
NU1000|Cu-tmpaCOOH batch 1 after CA	11 : 2	1.2 (±0.1)
NU1000|Cu-tmpaCOOH batch 2	8 : 1	0.8 (±0.0)
NU1000|$Cu(OTf)_2$	9 : 1	0.7 (±0.1)

[a] average of three measurements with the mean deviation from the average between brackets

2.2.3 Electrochemical behavior

Activity

The activity of NU1000|Cu-tmpaCOOH towards electrochemical O_2 reduction was studied with cyclic voltammetry (CV) (Figure 2.6 and Figure 2.7) and chronoamperometry (CA) (Figure 2.7b). An ink containing the MOF, carbon black, Nafion® and acetone was drop casted onto a glassy carbon working electrode and allowed to dry before measurements. The CV of NU1000|Cu-tmpaCOOH in absence of oxygen gas showed a quasi-reversible wave at 0.24 V vs. RHE that is assigned to the $Cu^{II/I}$ redox couple. When the Cu-tmpaCOOH catalyst is dissolved in the electrolyte rather than embedded in a MOF, a reversible wave is found at 0.24 V. vs RHE as well (Figure A2). A similar $Cu^{II/I}$ equilibrium potential of 0.21 V vs. RHE was reported for Cu-tmpa.[27] The quasi-reversible character of the redox event observed for NU1000|Cu-tmpaCOOH is expected to be caused by slow electron and electrolyte transport through the framework. Peak-to-peak separation increases with increasing scan rate (Figure 2.6b) and the Laviron plot (Figure 2.6c) is trumpet shaped, which is typical for a system in which electron transfer is rate limiting.[59] Slow mass and charge transport are effects previously described for electrocatalytic applications of several metal organic frameworks.[60–62] Charge transport in MOFs is governed by electron hopping coupled to cation migration and therefore greatly depends on diffusion of the cation through the framework. Integration of the reductive wave shows that 0.23 nmol electrons were

transferred. Since the reduction of Cu^{II} to Cu^{I} involves a single electron, 0.23 nmol Cu centers (3.25 nmol cm^{-2}) are activated in this CV. In a homogeneous solution only a small fraction of catalyst can be activated during catalysis (0.045 nmol cm^{-2} in Figure A2), while most of the catalytic species remain unaltered in the bulk solution.[63] By immobilization of homogeneous catalysts in MOFs a significantly larger number of catalytic sites is close to the electrode, and therefore a significantly lower number of catalytic sites remains unaffected during electrochemical experiments and applications.

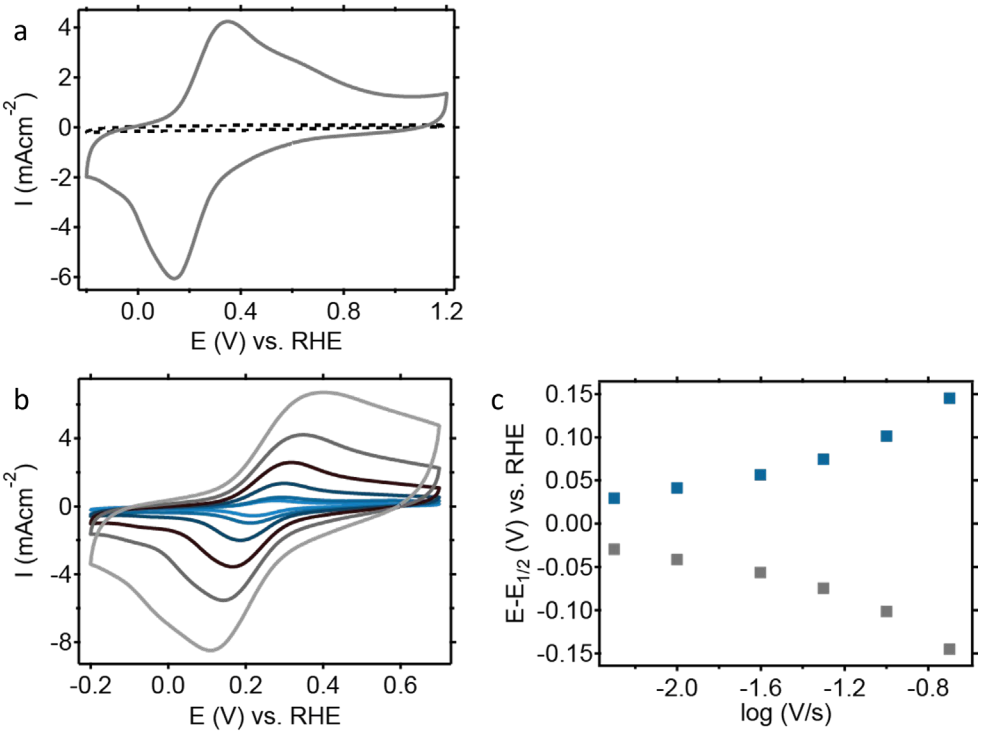

Figure 2.6 Cyclic voltammograms of a glassy carbon electrode under argon (a, black dashed line), NU1000|Cu-tmpaCOOH on a glassy carbon electrode under argon (a, grey line) at a scan rate of 100 mV s^{-1} and CV of NU1000|Cu-tmpaCOOH at scan rates ranging from 5 mV s^{-1} (b, light blue line) to 200 mV s^{-1} (b, light grey line) and corresponding Laviron plot (c).

Under an oxygen atmosphere, a catalytic wave with an onset potential ($i_p/i_{cat} \geq 2$) of 0.33 V vs. RHE appears (Figure 2.7a). The catalytic wave reaches a reductive peak current density of −40 $mAcm^{-2}$. Even though caution should be taken when comparing current densities of vastly different catalytic systems, a reductive current density of −40 $mAcm^{-2}$ is competitive with the state-of-the-art of oxygen reduction MOFs. Iron and cobalt porphyrin PCN MOFs with catalysts as every linker reached current densities of −2 $mAcm^{-2}$, albeit at a more

positive potential of 0.8 V vs. RHE,[34–37] while a zinc MOF resulted in −2.5mA cm^{-2}.[54] Copper catalysts directly attached to, or drop casted on electrodes, reached current densities of −0.6 $mAcm^{-2}$ and −5 $mAcm^{-2}$, respectively.[26,64] In the case of NU1000|Cu-tmpaCOOH the peak current of the catalytic wave is directly proportional to catalyst loading in the MOF for the two different MOF batches used in this work (Figure A3). Chronoamperometry (CA) was measured at 0.3 V vs. RHE for 6 hours under constant bubbling of O_2, resulting in a stable catalytic current of −7.5 $mAcm^{-2}$ (Figure 2.7b) for a dropcast that contained 97 nmol Cu-tmpaCOOH. A homogeneous solution of 5 µM Cu-tmpa (250 nmol) yielded a current density of −1 $mAcm^{-2}$.[65]

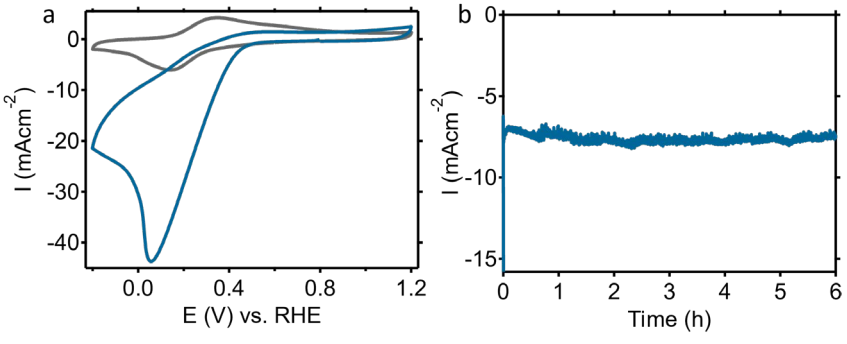

Figure 2.7 Cyclic Voltammetry of NU1000|Cu-tmpaCOOH on a glassy carbon electrode in 0.1 M phosphate buffer pH =7 under argon atmosphere (a, grey line) and under oxygen atmosphere (a, blue line) and chronoamperometry at 0.3 V vs. RHE of NU1000|Cu-tmpaCOOH on a glassy carbon electrode under constant bubbling of oxygen gas (b, blue line) in a 0.1 M phosphate buffer of pH 7. CVs are measured at a scan rate of 100 mV s^{-1}.

Stability

A CV taken after CA (Figure 2.8a) shows that a new, quasi-reversible redox couple has appeared and the peak current of the original redox couple has decreased. Additionally, ICPMS analysis of the drop cast shows lower amounts of Cu to be present in the MOF after the CA experiment compared to ICPMS analysis before the measurement (Table 2.1). Both observations can be explained by leaching of Cu from the MOF.[42,66,67] The additional redox couple measured after CA shows a great similarity with the redox couple measured previously for NU1000 with Cu nanoparticles,[56] as well as the redox wave in NU1000|$Cu(OTf)_2$ (Figure 2.8b). This suggests that Cu particles are formed during the catalytic reaction. However, the catalytic performance of NU1000|$Cu(OTf)_2$ for the oxygen reduction reaction is significantly lower than that of NU1000|Cu-tmpaCOOH (Figure 2.8c,d). This suggests that the tmpaCOOH ligand is essential for catalytic activity, which may be

explained by either Cu-tmpaCOOH itself being the catalytic site or by it playing an essential role in electron transport to the catalytic site.

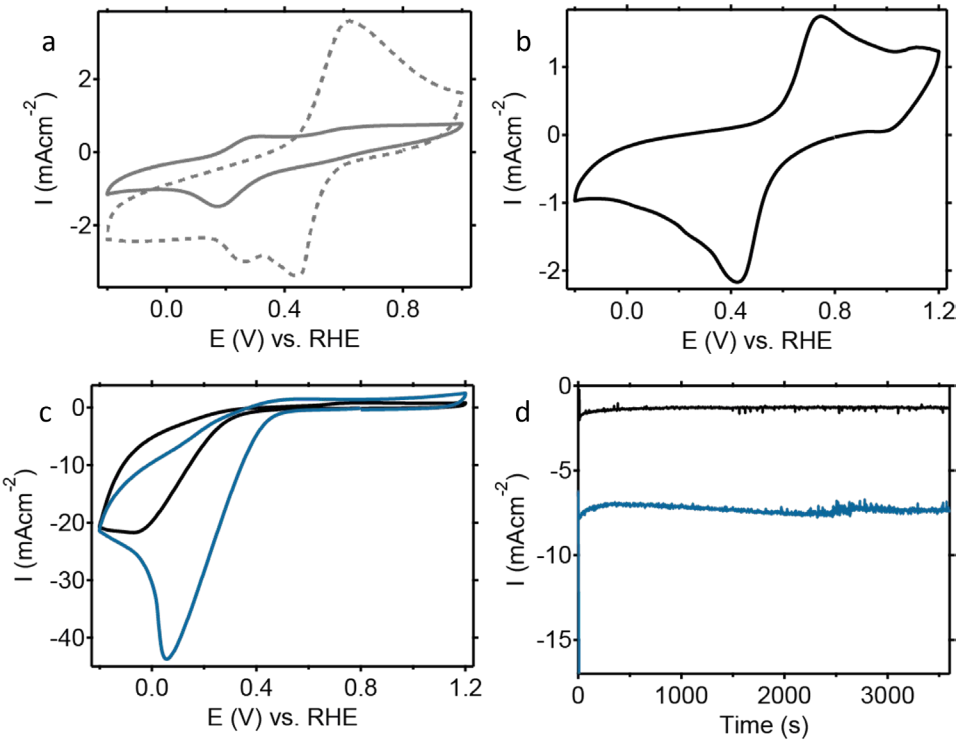

Figure 2.8 CV of NU1000|Cu-tmpaCOOH on a glassy carbon electrode in 0.1M PB pH = 7 under argon before (a, solid grey line) and after (a, dashed grey line) chronoamperometry at 0.3 V vs. RHE under O_2 atmosphere for 6 hours, with a 0.8 catalyst to node loading and CV under argon of NU1000|$Cu(OTf)_2$ on a glassy carbon electrode with a Cu to node loading of 1.5 (b). CV (c) and CA (d) of NU1000|Cu-tmpaCOOH (blue line) and NU1000|$Cu(OTf)_2$ (black line) on a glassy carbon electrode under oxygen atmosphere. CVs were measured at a scan rate of 50 mV s^{-1} and CA was measured at 0.3 V vs. RHE.

Recycling experiments (Figure 2.9) show stable catalytic current densities of ± −4.0 $mAcm^{-2}$ that could be obtained with the same electrode in five consecutive days. The electrode was held at open circuit potential (OCP) overnight between measurements. The stable catalytic currents illustrate that the catalytic activity of NU1000|Cu-tmpaCOOH can be maintained despite some initial leaching of copper and indicate reusability of the MOF. The reusability of the Cu-tmpaCOOH is improved compared to a homogeneous solution of Cu-tmpa, which showed significant loss of current density over 28 h CA divided over three days.[65] The catalytic signal of NU1000|Cu-tmpaCOOH is exceptionally stable compared to the PCN

MOFs mentioned before, which were shown to have significant loss of activity over 3-6 hours of chronoamperometry experiments.[34–37]

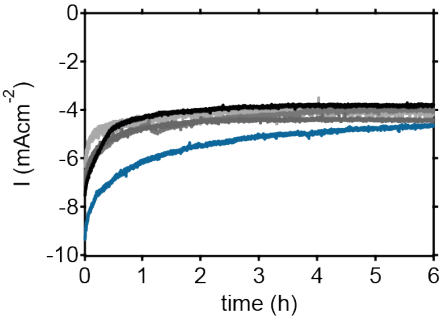

Figure 2.9 Reusability experiments of NU1000|Cu-tmpaCOOH on a glassy carbon electrode in 0.1M PB pH =7 under 1 atm oxygen at 0.3 V vs. RHE. Chronoamperometry was measured for 6 hours, followed by storing the electrode in electrolyte at OCP overnight and reusing the same electrode for the next CA experiment. Blue line = day 1, grey lines = day 2-4, black line = day 5. MOF with a loading of 0.8 catalysts per node was used for this experiment.

Selectivity

The concentration of H_2O_2 formed by NU1000|Cu-tmpaCOOH was measured in fivefold with a reflectometer and reflectometer peroxide-test strips. After 6 hours, a H_2O_2 concentration of 0.21 µmol was found, with a standard deviation of 0.02 µmol of two separate 6h CA measurements. The H_2O_2 concentration of 0.21 µmol was obtained with a current density of −3.5 $mAcm^{-2}$ for 6 hours and translates to a Faradaic Efficiency (FE) that lies below 1%. As only a small portion of the current eventually ends up in H_2O_2, the ORR by this MOF is expected to favor water as the ORR product.

Rotating Disk Electrode (RDE) and Rotating Ring Disk Electrode (RRDE) measurements were performed to further investigate the selectivity of the ORR. Cyclic voltammograms at rotation speeds ranging from 400 rpm (Figure 2.10a, black line) to 2800 rpm (Figure 2.10a, dark blue line) were measured and the limiting currents (at −0.35 V vs. RHE) were plotted in a Koutecky-Levich (K-L) diagram (Figure 2.10b). The electron-transfer number (n) was calculated using the K-L equation (Appendix A5).[37,68] Solving this equation resulted in n = 4.3, which indicates that four electrons are transferred per O_2 molecule, and illustrates that H_2O is the main product of the ORR. A similar value of n = 4.4 was found for Cu-tmpaCOOH in solution (Appendix A6). RRDE experiments with a Pt disk with the same size were shown to give a limiting current density of −7 $mAcm^{-2}$ in previous work.[27] As platinum is known to transfer four electrons to form water as the only product of oxygen reduction, finding

similar limiting currents in case of Pt and NU1000|Cu-tmpaCOOH is in good agreement with the observed n-values.

The CV at 400 rpm in Figure 2.10a shows a feature at 0.2 V vs. RHE that is distinct for substrate depletion. With increasing rotation speed, the feature becomes less pronounced and completely disappears at 2000 rpm. A possible explanation for this is that at low rotation rates the oxygen in the pores is consumed before new oxygen is supplied, causing the peak shaped feature in the CV. Therefore, by increasing rotation speed, and thereby mass transport, the feature disappears. The amount of oxygen supplied by rotation is determining for the current density of the plateau.

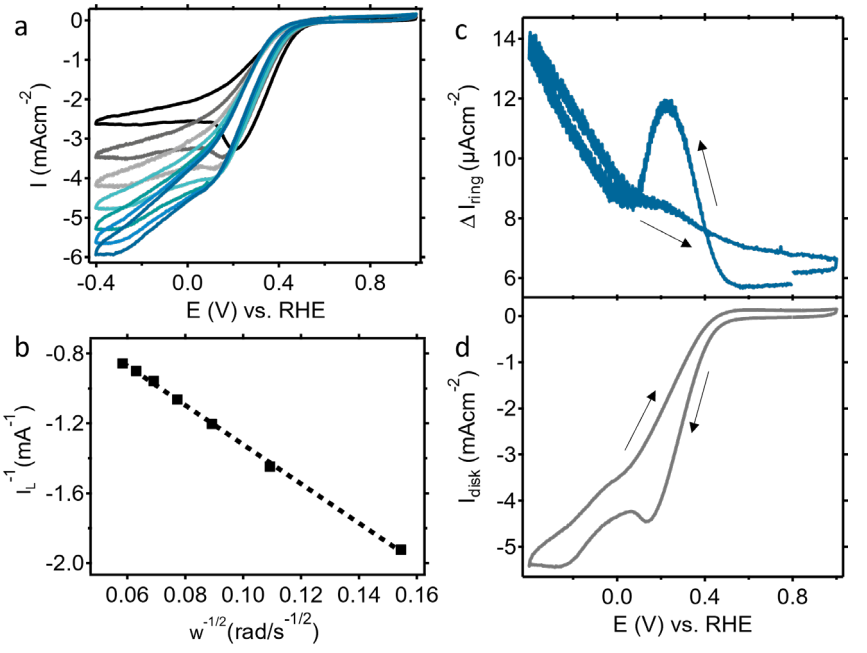

Figure 2.10 RDE cyclic voltammograms of NU1000|Cu-tmpaCOOH at scan rates ranging from 400 rpm (a, black line) to 2800 rpm (dark blue line), Koutecky-Levich plot (b) of datapoints at −0.35 V vs. RHE (R^2=0.999) and RRDE cyclic voltammograms at 1600 rpm (c, ring current and d, disk current) at a scan rate of 50 mV s^{-1}. 100 µg of MOF with 0.8 catalysts per node was dropcasted on a glassy carbon disk with a platinum ring around.

The amount of H_2O_2 produced was quantitatively analyzed with RRDE (Figure 2.10) using a glassy carbon disk (0.1963 cm^2) and a platinum ring (0.4398 cm^2). The currents measured at the ring (I_r) and disk (I_d) were used to calculate the FE for H_2O_2 using Equation 4:

$$FE\ (H_2O_2)\ \% = (200\ I_r / N)\ (I_d + I_r / N)^{-1} \qquad (4)$$

Where N is the collection efficiency of H_2O_2 at the ring. A maximum faradaic efficiency of 10% for H_2O_2 in both CV and CA (at 0.3 V vs. RHE) measurements was found (Figure 2.11). The FE (H_2O_2) values found for RRDE and for directly measuring H_2O_2 concentration are significantly lower than values of 75-90% previously reported for Cu-tmpa in solution,[27] and of 45% for Cu-tmpaCOOH in solution (Figure 2.11 and Figure A6). The relatively lower quantity of H_2O_2 observed for NU1000|Cu-tmpaCOOH is likely the result of either no H_2O_2 being formed and the ORR proceeding via a direct 4-electron reduction towards water (Equation 1), or as the result of fast follow up reactions involving the H_2O_2 formed (Equation 2, 3 and 5).

$$2H_2O_2 \longrightarrow 2H_2O + O_2 \qquad (5)$$

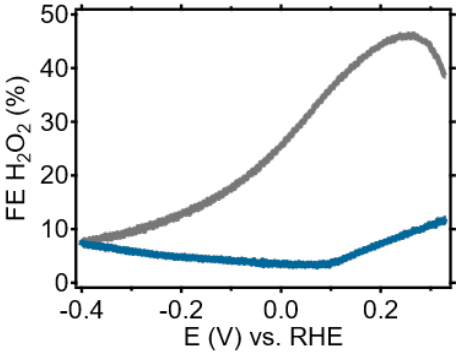

Figure 2.11 Faradaic Efficiency for H_2O_2 in the ORR by 0.3 mM Cu-tmpaCOOH (grey line) and NU1000|Cu-tmpaCOOH (blue line) as determined by RRDE experiments in Figures 2.10 and Figure A6 during CV. The first scan, starting at the O_2 reduction onset at 0.33 V vs. RHE, to −0.4 V vs. RHE is shown.

In order to investigate whether NU1000|Cu-tmpaCOOH is able to reduce any H_2O_2 that is formed, CV and CA of H_2O_2 reduction were measured (Figure 2.12) and the H_2O_2 concentrations before and after CA were determined with reflectometry (Table 2.2). After 60 minutes of chronoamperometry, 0.03 mmol of H_2O_2 was consumed, which equals transfer of 0.06 mmol electrons, according to Equation 3. However, the total charge transferred after 60 minutes was 1.08 C, which corresponds to 0.01 mmol electrons transferred. In other words, the amount of H_2O_2 consumed was six-fold compared to the maximum amount theoretically possible if the decomposition of H_2O_2 would only occur through electrocatalysis. This strongly suggests that disproportionation of H_2O_2 must be

taking place, as previously reported to be catalyzed by molecular Cu catalysts.[25,69,70] Control experiments illustrate that the H_2O_2 concentration does not decrease over time in absence or in presence of the NU1000|Cu-tmpaCOOH electrode if no potential is applied. Apparently, disproportionation of H_2O_2 only occurs when a reductive potential is applied, suggesting that reduced Cu species embedded within the MOF are responsible for this reaction.

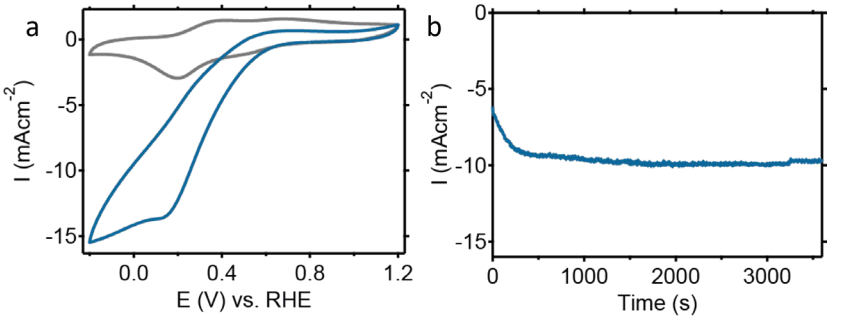

Figure 2.12 Cyclic voltammograms of NU1000|Cu-tmpaCOOH on a glassy carbon electrode under argon without (a, grey line) and with 7.5 mM H_2O_2 (a, blue line) and chronoamperometry (b) at 0.3 V vs. RHE of NU1000|Cu-tmpaCOOH on a glassy carbon electrode in presence of 7.5 mM H_2O_2. CVs are measured at a scan rate of 100 mV s^{-1}.

Table 2.2 Concentrations of hydrogen peroxide in electrolyte solutions before and after H_2O_2 reduction. Concentrations are an average of four measurements with an RQflex 20 reflectometer and reflectometer 0.2-20 mg/L peroxide-test strips.

Electrolyte solution	**H_2O_2 concentration (mM)**
Solution at start	10.6 (±0.3)
Solution after 60 minutes	10.9 (±0.2)
Solution after 60 minutes exposure to a **NU1000|Cu-tmpaCOOH** electrode, no potential applied.	10.6 (±0.3)
Solution after 60 minutes CA at 0.3 V vs. RHE	7.6 (±0.05)

The electrocatalytic ORR mediated by NU1000|Cu-tmpaCOOH may occur via a direct 4-electron reduction reaction (eq. 1), or via the sequential reduction of O_2 to H_2O_2 (eq. 2) followed by either reduction of H_2O_2 to H_2O (eq. 3) or disproportionation of H_2O_2 (eq. 5). The first of these possible mechanisms is unlikely, as the direct 4-electron reduction towards water requires the accumulation of 4 reductive equivalents, which seems unlikely to occur for a single site Cu-tmpa catalyst. However, the redox couple found after catalysis (Figure 2.8a) suggests the formation of Cu-nanoparticles, which may have a different selectivity for the ORR. The catalytic centers in NU1000|Cu-tmpaCOOH are confined in pores and are not

in close enough proximity for formation of dimers, as node-to-node distances in NU1000 are larger than the size of a Cu-tmpaCOOH catalyst (Appendix A6). However, it is difficult to fully rule out mobility of the Cu-centers under reductive conditions.

The altered selectivity of NU1000|Cu-tmpaCOOH compared to Cu-tmpa for the ORR can be either an effect of confinement of the catalyst, or a change in the active species. The latter will be investigated in Chapter 3. The ORR mediated by Cu-tmpa in solution was previously shown to occur via H_2O_2 as an isolable intermediate.[27,28] Although we cannot be certain that an immobilized catalyst operates via the same pathways as in solution,[46] NU1000|Cu-tmpaCOOH and Cu-tmpaCOOH electrochemically behave very similar (Figure 2.7 and A2). NU1000|Cu-tmpaCOOH shows the same 1st order substrate concentration dependence as was reported for Cu-tmpa (Figures A4 and A5).[27,28] Additionally, disproportionation of peroxide evidently plays a role when significant concentrations of hydrogen peroxide are present. As the disproportionation of hydrogen peroxide is expected to be second order in substrate,[70] it will likely contribute more to H_2O_2 clearance at high H_2O_2 concentrations. Additionally, Foot Of the Wave Analysis (FOWA) of the homogeneous Cu-tmpaCOOH catalyst (Appendix A7) shows that the hydrogen peroxide reduction reaction catalyzed by Cu-tmpaCOOH is slightly faster (TOF_{max} =6.8 $\times$ 10^4 ($\pm$ 0.6 $\times$ 10^4) s^{-1}) than the oxygen reduction reaction (TOF_{max} = 3.7 $\times$ 10^4 ($\pm$ 1.1 $\times$ 10^4) s^{-1}) at equal substrate concentrations (Appendix A7). This contrasts with results obtained with Cu-tmpa, for which the oxygen reduction reaction is significantly faster than the further reduction of hydrogen peroxide.[27,28] This suggests that Cu-tmpaCOOH is already slightly more biased towards the production of water.

Most importantly, the MOF pores form a confined environment from which reactants cannot diffuse away easily.[62] H_2O_2 diffusing out of the MOF cannot occur without passing several catalytic centers. The retention of formed hydrogen peroxide in the MOF pores close to the catalytic center, combined with a higher catalytic rate of reduction of H_2O_2 to water and higher H_2O_2 clearance by disproportionation, would result in quick clearance of formed hydrogen peroxide. This would explain the low amounts of hydrogen peroxide observed in our experiments, as was particularly evident from the stationary bulk electrolysis experiments. Overall, we can conclude that the confinement of the Cu catalyst in NU1000 pores creates a catalytic system which directs the oxygen reduction reaction towards the selective production of water. The identification of the active species responsible for this shift in observation is the focus of Chapter 3.

2.3 Conclusion

The homogeneous oxygen reduction electrocatalyst Cu-tmpaCOOH was incorporated in the NU1000 metal organic framework by Solvent-Assisted Ligand Incorporation (SALI). The resulting MOF NU1000|Cu-tmpaCOOH selectively reduces molecular oxygen to water, with excellent catalytic rates and overall stability of the electrocatalyst. Hydrogen peroxide is a likely intermediate, yet its concentration does not build up because of its retention in the MOF pores and rapid hydrogen peroxide reduction mediated by the MOF incorporated catalyst. This work demonstrates that the confinement of a catalyst and substrate in MOF pores enables one to steer the ORR selectivity to water. Ultimately, it is shown that the selectivity of electrochemical reactions can be directed without conceding on the catalytic activity by incorporating a molecular catalyst into a MOF, which offers potential for a wide variety of electrochemical conversions that are relevant to the energy transition.

2.4 Experimental

2.4.1 Materials

Chemicals were purchased from commercial suppliers and used without further purification. DCM and CH_3CN were dried using a PureSolve 400 solvent dispenser. Other dry solvents (dichloroethane (EDC, dioxane) were dried on molecular sieves (3Å) and degassed by bubbling N_2 for 15 min. Reaction flasks were degassed by 3 vacuum/N_2 cycles. Phosphate buffer was prepared using NaH_2PO_4 (Suprapur®, Merck) and Na_2HPO_4 (Suprapur®, Merck). Elemental analysis was performed by Mikroanalytisches Laboratorium Kolbe. Milli-Q Ultrapure grade water (>18.2 MΩ cm resistivity) was used for all electrochemical experiments and for the preparation of buffer. Hydrogen peroxide quantification was performed using a RQflex 20 reflectometer purchased from Sigma Aldrich and reflectometer 0.2-20 mg/L peroxide-test strips (0.2-20 mg/L concentration range with a standard deviation of 0.2 mg/L) purchased from VWR avantor. 5.0 grade H_2, O_2 and Ar gasses were purchased from Linde.

2.4.2 Physical Characterization

^1H and ^{13}C NMR spectra were measured using a Bruker AV400 MHz spectrometer. Powder XRD spectra were measured on a Rigaku Miniflex II desktop X-ray diffractometer with 0.05° steps and a speed of 1°/min. N_2-adsorption isotherm was measured on a Belsorp II max.

SEM images were recorded on a JSM-7600F field emission scanning electron microscope from Jeol, with a 20 mm working distance. FT-IR spectra were measured on a Spectrum Two FT-IR spectrometer from Perkin Elmer. EPR spectra were recorded of Cu-tmpa, Cu-tmpaCOOH and NU1000|Cu-tmpaCOOH in quartz glass EPR tubes on a Bruker EMX EPR spectrometer. The temperature was kept constant at 130 K, controlled with a variable Temperature unit BVT3000, and the spectra recorded under a continuous flow of nitrogen gas. The nitrogen gas was cooled by passing the gas through liquid nitrogen (77 K). ICPMS samples were prepared by digesting 150 µg of MOF in 5 mL 67 % nitric acid at 120˚C overnight. 144 µL of the resulting solution was added to 9.85 mL of Milli-Q water. ICPMS was measured on a NexION® 2000 ICP Mass Spectrometer from Perkin Elmer N_2-adsorption isotherm was measured on a Belsorp II max. SEM images were recorded on a JSM-7600F field emission scanning electron microscope from Jeol, with a 20 mm working distance. FT-IR spectra were measured on a Spectrum Two FT-IR spectrometer from Perkin Elmer. EPR was measured on a Bruker EMX EPR spectrometer and the temperature controlled with a variable Temperature unit BVT3000. ICPMS was measured on a NexION® 2000 ICP Mass Spectrometer from Perkin Elmer.

2.4.3 Electrochemistry

A PEEK encapsulated glassy carbon working electrode with 3 mm diameter (0.07069 cm^2 surface area) from Metrohm was polished for 2 minutes with DiaPro water-based diamond suspension, followed by 2 minutes with OP-S NonDry colloidal silica suspension, on a Struers LaboPol-20 polishing machine. The electrode was then sonicated in Milli-Q for 15 minutes and rinsed with acetone before drop casting. A mixture of 2 mg NU1000|Cu-tmpaCOOH, 1 mg carbon black, 20 µL Nafion® perfluorinated resin solution in propanol and 180 µL HPLC-grade acetone was sonicated for 15 minutes and shortly vortexed. A 15 µL sample was drop casted onto the GC electrode with a microman E M100 organic solvents pipet from Gilson. The electrode was allowed to dry for 15 minutes before use. Autolab PGSTAT 12 and Autolab PGSTAT 128N potentiostats were used in combination with Autolab NOVA software. A custom made, one compartment electrochemical cell with three electrode setup was used. All glassware was cleaned overnight in an aqueous 0.5 M H_2SO_4 solution with 1 mg/mL $KMnO_4$. Excess $KMnO_4$ was removed from the glassware with a diluted solution of H_2SO_4 and H_2O_2, followed by boiling (3 × 30 min.) in Milli-Q. A gold wire was used as the counter electrode, a platinum mesh electrode with H_2 bubbling was used as a reversible hydrogen reference electrode and a platinum wire was used as a capacitor. The Pt mesh electrode was cleaned by boiling in Milli-Q for 15 minutes and the Au and Pt wires

were cleaned by flame annealing. For R(R)DE measurements, a Pine instruments AFMSRCE modulated speed rotator, a GC disk with 5 mm diameter (0.1963 cm^2 surface area) and a Pt ring with 7.5 mm outer diameter and 6.5 inner diameter (0.4398 cm^2 surface area) were used. Phosphate buffer (0.1M) pH = 7 was used as the electrolyte for all electrochemical measurements. Solutions were degassed by bubbling argon for 15 minutes, after which an argon flow over the solution was maintained during measurements. Solutions were saturated with 1.2 mM oxygen by bubbling 15 minutes with oxygen, after which an oxygen flow over the solution was maintained during measurements.

2.4.4 Synthetic protocols

*Methyl-6-formyl nicotinate (**1**)*

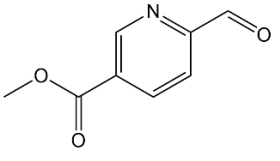

Methyl-6-formyl nicotinate (**1**) was synthesized according to a literature procedure.[71] Methyl 6-hydroxymethylnicotinate (1.0 g, 5.98 mmol) was dissolved in 90 mL dry DCM under nitrogen atmosphere. Dess Martin periodinane (3.04 g, 7.18 mmol) in 10 mL dry DCM was added slowly and the solution stirred at RT overnight. Complete conversion was confirmed by TLC (petroleum ether : ethyl acetate (3 : 1), rf = 0.5), and the reaction quenched with water (100 mL), followed by extraction of the product with ethyl acetate (3 × 100 mL). The combined organic phases were dried on $MgSO_4$, filtered and concentrated to yield **1** as a white solid. Yield: 100% (988 mg, 5.98 mmol). ^{1}H NMR (400 MHz, $CDCl_3$) δ 10.10 (s, 1H), 9.32 (s, 1H), 8.44 (dt, J = 8, 1 Hz, 1H), 7.99 (d, J = 8 Hz, 1H), 3.96 (d, J = 0.9 Hz, 3H). ESI MS m/z (calc): 198.2 (198.2, $[M + MeOH + H^+]^+$).

*Methyl 6-bis(pyridin-2-ylmethyl)aminomethylnicotinate (tmpaCOOMe) (**2**)*

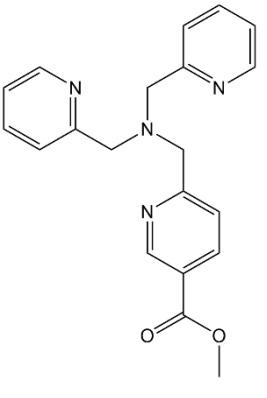

TmpaCOOMe (**2**) was synthesized according to a procedure adjusted from literature.[27,72] Methyl 6-formylnicotinate (1) (497 mg, 3.01 mmol) and bis(pyridin-2-ylmethyl)amine (0.54 mL, 3.01 mmol) were dissolved in 14 mL dry ethylene dichloride (EDC) with mol sieves (3Å) under N_2 atmosphere. Sodium triacetoxyborohydride (957 mg, 4.52 mmol) was added to the solution, followed by acetic acid (0.172 ml, 3.01 mmol) and the mixture was stirred for 3 days. The reaction was quenched with sat. $NaHCO_3$ (50 mL). The mixture was extracted with EtOAc (3 × 50 mL) and the organic layer was washed with saturated $NaHCO_3$ (50 mL). The organic layers were dried with $NaSO_4$ and filtered over a glass frit. The solvent

was removed by rotary evaporation to obtain a dark yellow oil. The crude was chromatographed on silica gel eluting with ethyl acetate : methanol (4 : 1) (rf: 0.1) to yield **2** as a dark yellow oil. Yield: 43% (449 mg, 1.29 mmol). ^{1}H NMR (400 MHz, $CDCl_3$) δ 9.03 (dd, J = 2.16, 0.8 Hz, 1H), 8.45 (dq, J = 4.86, 0.9 Hz, 2H), 8.16 (dd, J = 8.22, 2.22 Hz, 1H), 7.61 (d, J = 8.26 Hz, 1H), 7.57 (td, J = 7.74, 1.85 Hz, 2H), 7.45 (d, J = 7.8 Hz, 2H), 7.06 (ddd, J = 7.34, 4.82, 1.22 Hz, 2H), 3.86 (s, 2H), 3.83 (s, 3H), 3.80 (s, 4H). ^{13}C NMR (400 MHz, $CDCl_3$) δ 165.78 (C_q), 164.18 (C_q), 158.89 (2 x C_q), 150.30 (CH), 149.17 (2 x CH), 137.47 (CH), 136.48 (2 x CH), 124.39 (C_q), 123.01 (2 x CH), 122.40 (CH), 122.13 (2 x CH), 60.24 (2 x CH_2), 59.94 (CH_2), 52.28 (CH_3). ESI MS m/z (calc): 349.1 (349.1, $[M + H^+]^+$).

*6-bis(pyridin-2-ylmethyl)aminomethylnicotinic acid (tmpaCOOH) (**3**)*

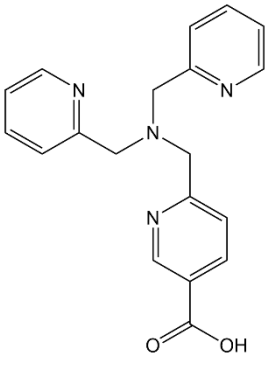

TmpaCOOH (**3**) was obtained from tmpaCOOMe (**2**) by a procedure adjusted from literature.[73] TmpaCOOMe (2) (250 mg, 0.718 mmol) was dissolved in 50 mL THF : H_2O (4 : 1),5 eq. of LiOH (mg, mmol) added and the mixture stirred at RT overnight. THF was evaporated by rotary evaporation and the water layer acidified to pH = 3 by adding concentrated HCl dropwise. The aqueous layer was then washed with DCM (3 × 50 mL). Water was evaporated and the resulting solid was sonicated in CH_3Cl (5 × 50 mL). The CH_3Cl fractions were combined and concentrated to yield **3** as an off-white solid. Yield: 67% (160 mg, 0.478 mmol). ^{1}H NMR (400 MHz, D_2O) δ 9.21 (dd, J = 2.08, 0.66 Hz, 1H), 8.87 (dd, J = 8.35, 1.98 Hz, 1H), 8.73 (ddd, J = 5.90, 1.64, 0.66 Hz, 2H), 8.51 (td, J = 8.00, 1.58 Hz, 2H), 8.19 (dd, J = 8.30, 0.46 Hz, 1H), 8.11 (d, J = 7.89 Hz, 2H), 7.95 (ddd, J = 7.89, 5.84, 1.22 Hz, 2H), 4.46 (s, 2H), 4.43 (s, 4H). ^{13}C NMR (400 MHz, D_2O) δ 165.09 (C_q), 155.35 (C_q), 150.89 (2 x C_q), 147.68 (2 x CH), 146.48 (CH), 144.29 (CH), 141.83 (2 x CH), 129.70 (C_q), 127.72 (2 x CH), 127.38 (CH), 126.87 (2 x CH), 56.70 (CH_2), 56.20 (2 x CH_2). ESI HR-MS m/z (calc): 335.1 (335.1, $[M + H^+]^+$). Elemental analysis for $C_{19}H_{18}N_4O_2 \bullet 0.3H_2O$: (calcd.): C, 67.16; H, 5.52; N,16.49; (exp.): C, 67.37; H, 5.91, N, 16.12.

[Cu-tmpaCOOH(OTf)]OTf

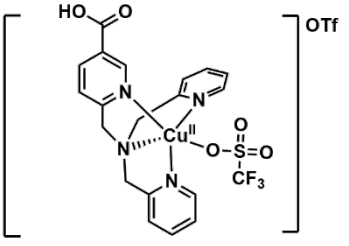

TmpaCOOH (3) (135 mg, 0.404 mmol) and $Cu(OTf)_2$ (131 mg, 0.363 mmol) were dissolved in dry CH_3CN (10 mL) under N_2 atmosphere and the resulting dark green mixture was stirred for 1h. CH_3CN was evaporated by rotary evaporation and the resulting solid was recrystallized from CH_3CN (1 mL) and Et_2O (20 mL) by vapor diffusion to yield a hygroscopic dark green solid in 81% yield (204 mg, 293 mmol). Evans ^1H NMR (400 MHz, D_2O : dioxane (9:1); μ_{eff} = 1.95, corresponding to 1 unpaired electron. ESI HR-MS m/z (calc): 335.1 (442.1, $[M^{2+} + CHOO^-]^+$). Elemental analysis for $C_{21}H_{18}CuF_6N_4O_8S_2 \bullet 0.35H_2O$: (calcd.): C, 35.91; H, 2.68; N, 7.98; (exp.): C, 35.93; H, 2.62, N, 7.98.

4,4',4'',4'''-(pyrene-1,3,6,8-tetrayl)tetrabenzoic acid (H_4TBAPy)

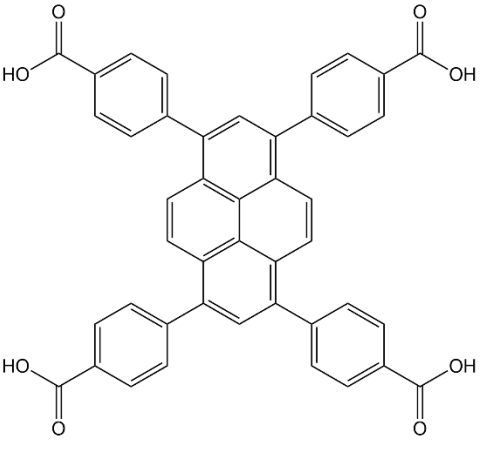

4,4',4'',4'''-(pyrene-1,3,6,8-tetrayl) tetrabenzoic acid (H_4TBAPy) was synthesized according to a literature procedure,[74] in 44% yield (1.62 g, 2.38 mmol). ^1H NMR (400 MHz, DMSO-d6) δ 8.21 (s, 4H), 8.17 (d, J = 8.00 Hz, 8H), 8.08 (s, 2H), 7.86 (d, J = 8.40 Hz, 8H).

Synthesis of NU1000 and Solvent-Assisted Ligand Incorporation (SALI)

NU1000 was grown solvothermally as described in literature.[75] Formation of NU1000 MOF was confirmed by SEM and XRD measurements. NU1000 was then activated by heating to 120 °C overnight. To incorporate Cu-tmpaCOOH into the MOF, 150 mg of NU1000 was submerged in a 0.1 M solution of Cu-tmpaCOOH in DMF for 30 days at 60 °C. The MOF was spinned down by centrifugation with a Rotina 360R centrifuge from Hettich at 4000 rpm for 20 minutes and washed with DMF (3 × 50 mL) and DCM (3 × 50 mL). Formation of the MOF was confirmed by PXRD spectra and SEM images and incorporation of the catalyst was confirmed by ICPMS and EPR.

2.5 References

[1] G. Papanikolaou, G. Centi, S. Perathoner, P. Lanzafame, *ACS Catal* **2022**, 2861–2876.

[2] S. Perathoner, G. Centi, *Catal Today* **2019**, *330*, 157–170.

[3] G. Centi, S. Perathoner, *Catal Today* **2022**, *387*, 216–223.

[4] Y. Wang, H. Cui, Z. W. Wei, H. P. Wang, L. Zhang, C. Y. Su, *Chem Sci* **2016**, *8*, 775–780.

[5] Y. Ning, M. Wei, L. Yu, F. Yang, R. Chang, Z. Liu, Q. Fu, X. Bao, *Journal of Physical Chemistry C* **2015**, *119*, 27556–27561.

[6] K. Hemmer, M. Cokoja, R. A. Fischer, *ChemCatChem* **2021**, *13*, 1683–1691.

[7] X. Fei, P. Wang, D. Zhang, H. Wang, Z. Wu, *ChemCatChem* **2021**, *13*, 2313–2336.

[8] V. Mouarrawis, R. Plessius, J. I. van der Vlugt, J. N. H. Reek, *Front Chem* **2018**, *6*, 623.

[9] X. Gong, Y. Shu, Z. Jiang, L. Lu, X. Xu, C. Wang, H. Deng, *Angewandte Chemie International Edition* **2020**, *59*, 5326–5331.

[10] T. Uemura, R. Kitaura, Y. Ohta, M. Nagaoka, S. Kitagawa, *Angewandte Chemie International Edition* **2006**, *45*, 4112–4116.

[11] M. Zheng, Y. Liu, C. Wang, S. Liu, W. Lin, *Chem Sci* **2012**, *3*, 2623–2627.

[12] C. T. He, L. Jiang, Z. M. Ye, R. Krishna, Z. S. Zhong, P. Q. Liao, J. Xu, G. Ouyang, J. P. Zhang, X. M. Chen, *J Am Chem Soc* **2015**, *137*, 7217–7223.

[13] J. Canivet, S. Aguado, C. Daniel, D. Farrusseng, *ChemCatChem* **2011**, *3*, 675–678.

[14] A. Corma, M. J. Díaz-Cabãas, J. L. Jordá, C. Martínez, M. Moliner, *Nature* **2006**, *443*, 842–845.

[15] J. Wu, X. Z. Yuan, J. J. Martin, H. Wang, J. Zhang, J. Shen, S. Wu, W. Merida, *J Power Sources* **2008**, *184*, 104–119.

[16] M. L. Pegis, C. F. Wise, D. J. Martin, J. M. Mayer, *Chem Rev* **2018**, *118*, 2340–2391.

[17] P. Vasudevan, Santosh, N. Mann, S. Tyagi, *Transition Metal Chemistry* **1990**, *15*, 81–90.

[18] J. Zhang, F. C. Anson, *Journal of Electroanalytical Chemistry* **1992**, *341*, 323–341.

[19] J. Zhang, F. C. Anson, *Journal of Electroanalytical Chemistry* **1993**, *348*, 81–97.

[20] E. A. Lewis, W. B. Tolman, *Chem Rev* **2004**, *104*, 1047–1076.

[21] S. Kakuda, R. L. Peterson, K. Ohkubo, K. D. Karlin, S. Fukuzumi, *J Am Chem Soc* **2013**, *135*, 6513–6522.

[22] C. C. L. McCrory, X. Ottenwaelder, T. D. P. Stack, C. E. D. Chidsey, *Journal of Physical Chemistry A* **2007**, *111*, 12641–12650.

[23] M. Asahi, S. I. Yamazaki, S. Itoh, T. Ioroi, *Dalton Transactions* **2014**, *43*, 10705–10709.

[24] M. Asahi, S. I. Yamazaki, S. Itoh, T. Ioroi, *Electrochim Acta* **2016**, *211*, 193–198.

[25] M. A. Thorseth, C. S. Letko, T. B. Rauchfuss, A. A. Gewirth, *Inorg Chem* **2011**, *50*, 6158–6162.

[26] M. A. Thorseth, C. S. Letko, E. C. M. Tse, T. B. Rauchfuss, A. A. Gewirth, *Inorg Chem* **2013**, *52*, 628–634.

[27] M. Langerman, D. G. H. Hetterscheid, *Angewandte Chemie International Edition* **2019**, *58*, 12974–12978.

[28] M. Langerman, D. G. H. Hetterscheid, *ChemElectroChem* **2021**, *8*, 2783–2791.

[29] Y. Han, J. R. Li, Y. Xie, G. Guo, *Chem Soc Rev* **2014**, *43*, 5952–5981.

[30] M. R. Di Nunzio, V. Agostoni, B. Cohen, R. Gref, A. Douhal, *J Med Chem* **2014**, *57*, 411–420.

[31] P. Manna, J. Debgupta, S. Bose, S. K. Das, *Angewandte Chemie International Edition* **2016**, *55*, 2425–2430.

[32] B. A. Johnson, A. Bhunia, S. Ott, *Dalton Transactions* **2017**, *46*, 1382–1388.

[33] S. Pullen, S. Roy, S. Ott, *Chemical Communications* **2017**, *53*, 5227–5230.

[34] M. O. Cichocka, Z. Liang, D. Feng, S. Back, S. Siahrostami, X. Wang, L. Samperisi, Y. Sun, H. Xu, N. Hedin, H. Zheng, X. Zou, H. C. Zhou, Z. Huang, *J Am Chem Soc* **2020**, *142*, 15386–15395.

[35] N. Kornienko, Y. Zhao, C. S. Kley, C. Zhu, D. Kim, S. Lin, C. J. Chang, O. M. Yaghi, P. Yang, *J Am Chem Soc* **2015**, *137*, 14129–14135.

[36] T. F. Liu, D. Feng, Y. P. Chen, L. Zou, M. Bosch, S. Yuan, Z. Wei, S. Fordham, K. Wang, H. C. Zhou, *J Am Chem Soc* **2015**, *137*, 413–419.

[37] W. Yan, Q. Xing, O. Guo, H. Feng, H. Liu, P. Deshlahra, X. Li, Y. Chen, *ACS Appl Mater Interfaces* **2022**, *14*, 50761.

[38] P. Deria, J. E. Mondloch, E. Tylianakis, P. Ghosh, W. Bury, R. Q. Snurr, J. T. Hupp, O. K. Farha, *J Am Chem Soc* **2013**, *135*, 16801–16804.

[39] P. Deria, W. Bury, J. T. Hupp, O. K. Farha, *Chemical Communications* **2014**, *50*, 1965–1968.

[40] P. Deria, W. Bury, I. Hod, C. W. Kung, O. Karagiaridi, J. T. Hupp, O. K. Farha, *Inorg Chem* **2015**, *54*, 2185–2192.

[41] J. T. Hyde, K. Hanson, A. K. Vannucci, A. M. Lapides, L. Alibabaei, M. R. Norris, T. J. Meyer, D. P. Harrison, *ACS Appl Mater Interfaces* **2015**, *7*, 9554–9562.

[42] N. W. G. Smits, D. Den Boer, L. Wu, J. P. Hofmann, D. G. H. Hetterscheid, *Inorg Chem* **2019**, *58*, 13007–13019.

[43] R. Matheu, L. Francàs, P. Chernev, M. Z. Ertem, V. Batista, M. Haumann, X. Sala, A. Llobet, *ACS Catal* **2015**, *5*, 3422–3429.

[44] P. Garrido-Barros, R. Matheu, C. Gimbert-Suriñach, A. Llobet, *Curr Opin Electrochem* **2019**, *15*, 140–147.

[45] A. K. Das, M. H. Engelhard, R. M. Bullock, J. A. S. Roberts, *Inorg Chem* **2014**, *53*, 6875–6885.

[46] N. W. G. Smits, B. van Dijk, I. de Bruin, S. L. T. Groeneveld, M. A. Siegler, D. G. H. Hetterscheid, *Inorg Chem* **2020**, *59*, 16398–16409.

[47] V. Budhija, P. H. van Langevelde, K. B. Krause, B. Cula, D. G. H. Hetterscheid, M. Schwalbe, *Eur J Inorg Chem* **2023**, *26*, e202200743.

[48] S. T. Madrahimov, J. R. Gallagher, G. Zhang, Z. Meinhart, S. J. Garibay, M. Delferro, J. T. Miller, O. K. Farha, J. T. Hupp, S. T. Nguyen, *ACS Catal* **2015**, *5*, 6713–6718.

[49] D. Yang, S. O. Odoh, T. C. Wang, O. K. Farha, J. T. Hupp, C. J. Cramer, L. Gagliardi, B. C. Gates, *J Am Chem Soc* **2015**, *137*, 7391–7396.

[50] K. Zhang, S. Goswami, H. Noh, Z. Lu, T. Sheridan, J. Duan, W. Dong, J. T. Hupp, *J Photochem Photobiol* **2022**, *10*, 100111.

[51] H. Noh, C. W. Kung, K. I. Otake, A. W. Peters, Z. Li, Y. Liao, X. Gong, O. K. Farha, J. T. Hupp, *ACS Catal* **2018**, *8*, 9848–9858.

[52] E. M. Miner, S. Gul, N. D. Ricke, E. Pastor, J. Yano, V. K. Yachandra, T. Van Voorhis, M. Dincă, *ACS Catal* **2017**, *7*, 7726–7731.

[53] X. Chen, Y. Kondo, Y. Kuwahara, K. Mori, C. Louis, H. Yamashita, *Physical Chemistry Chemical Physics* **2020**, *22*, 14404–14414.

[54] V. Raut, B. Bera, M. Neergat, D. Das, *Journal of Chemical Sciences* **2021**, *133*, 1–9.

[55] T. C. Wang, N. A. Vermeulen, I. S. Kim, A. B. F. Martinson, J. Fraser Stoddart, J. T. Hupp, O. K. Farha, *Nat Protoc* **2016**, *11*, 149–162.

[56] C. W. Kung, C. O. Audu, A. W. Peters, H. Noh, O. K. Farha, J. T. Hupp, *ACS Energy Lett* **2017**, *2*, 2394–2401.

[57] S. Goswami, I. Hod, J. D. Duan, C.-W. Kung, M. Rimoldi, C. D. Malliakas, R. H. Palmer, O. K. Farha, J. T. Hupp, *J. Am. Chem. Soc* **2019**, *141*, 9.

[58] S. Kakuda, R. L. Peterson, K. Ohkubo, K. D. Karlin, S. Fukuzumi, *J Am Chem Soc* **2013**, *135*, 6513–6522.

[59] C. M. Hanna, C. D. Sanborn, S. Ardo, J. Y. Yang, *ACS Appl Mater Interfaces* **2018**, *10*, 13211–13217.

[60] S. Roy, V. Pascanu, S. Pullen, G. González Miera, B. Martín-Matute, S. Ott, *Chemical Communications* **2017**, *53*, 3257–3260.

[61] I. Stassen, N. Burtch, A. Talin, P. Falcaro, M. Allendorf, R. Ameloot, *Chem Soc Rev* **2017**, *46*, 3185–3241.

[62] B. A. Johnson, A. M. Beiler, B. D. McCarthy, S. Ott, *J Am Chem Soc* **2020**, *142*, 11941–11956.

[63] D. J. Cole-Hamilton, R. P. Tooze, in *Catalyst Separation, Recovery and Recycling* (Eds.: D.J. Cole-Hamilton, R.P. Tooze), Springer Netherlands, **2006**, pp. 1–8.

[64] S. Wang, X. Gao, X. Mo, D. L. Phillips, E. C. M. Tse, *ACS Catal* **2023**, *13*, 5599–5608.

[65] P. H. van Langevelde, D. G. H. Hetterscheid, *Chem Catalysis* **2024**, *4*, 101069.

[66] N. W. G. Smits, D. Rademaker, A. I. Konovalov, M. A. Siegler, D. G. H. Hetterscheid, *Dalton Transactions* **2022**, *51*, 1206–1215.

[67] B. Van Dijk, J. P. Hofmann, D. G. H. Hetterscheid, *Physical Chemistry Chemical Physics* **2018**, *20*, 19625–19634.

[68] J. Li, Y. Chen, Y. Tang, S. Li, H. Dong, K. Li, M. Han, Y. Q. Lan, J. Bao, Z. Dai, *J Mater Chem A Mater* **2014**, *2*, 6316–6319.

[69] F. Ghiretti, *Arch Biochem Biophys* **1956**, *63*, 165–176.

[70] M. Jezowska-Bojczuk, W. Leśniak, W. Bal, H. Kozlowski, K. Gatner, A. Jezierski, J. Sobczak, S. Mangani, W. Meyer-Klaucke, *Chem Res Toxicol* **2001**, *14*, 1353–1362.

[71] M. O. Cichocka, Z. Liang, D. Feng, S. Back, S. Siahrostami, X. Wang, L. Samperisi, Y. Sun, H. Xu, N. Hedin, H. Zheng, X. Zou, H. C. Zhou, Z. Huang, *J Am Chem Soc* **2020**, *142*, 15386–15395.

[72] A. F. Abdel-Magid, K. G. Carson, B. D. Harris, C. A. Maryanoff, R. D. Shah, *Journal of Organic Chemistry* **1996**, *61*, 3849–3862.

[73] Ø. Samuelsen, O. A. H. Åstrand, C. Fröhlich, A. Heikal, S. Skagseth, T. J. O. Carlsen, H. K. S. Leiros, A. Bayer, C. Schnaars, G. Kildahl-Andersen, S. Lauksund, S. Finke, S. Huber, T. Gjøen, A. M. S. Andresen, O. A. Økstad, P. Rongved, *Antimicrob Agents Chemother* **2020**, *64*, e02415-19.

[74] J. E. Mondloch, W. Bury, D. Fairen-Jimenez, S. Kwon, E. J. Demarco, M. H. Weston, A. A. Sarjeant, S. T. Nguyen, P. C. Stair, R. Q. Snurr, O. K. Farha, J. T. Hupp, *J Am Chem Soc* **2013**, *135*, 10294–10297.

[75] T. C. Wang, N. A. Vermeulen, I. S. Kim, A. B. F. Martinson, J. Fraser Stoddart, J. T. Hupp, O. K. Farha, *Nat Protoc* **2016**, *11*, 149–162.